Journal of
Materials Chemistry B

Materials for biology and medicine

rsc.li/materials-b

ROYAL SOCIETY
OF CHEMISTRY
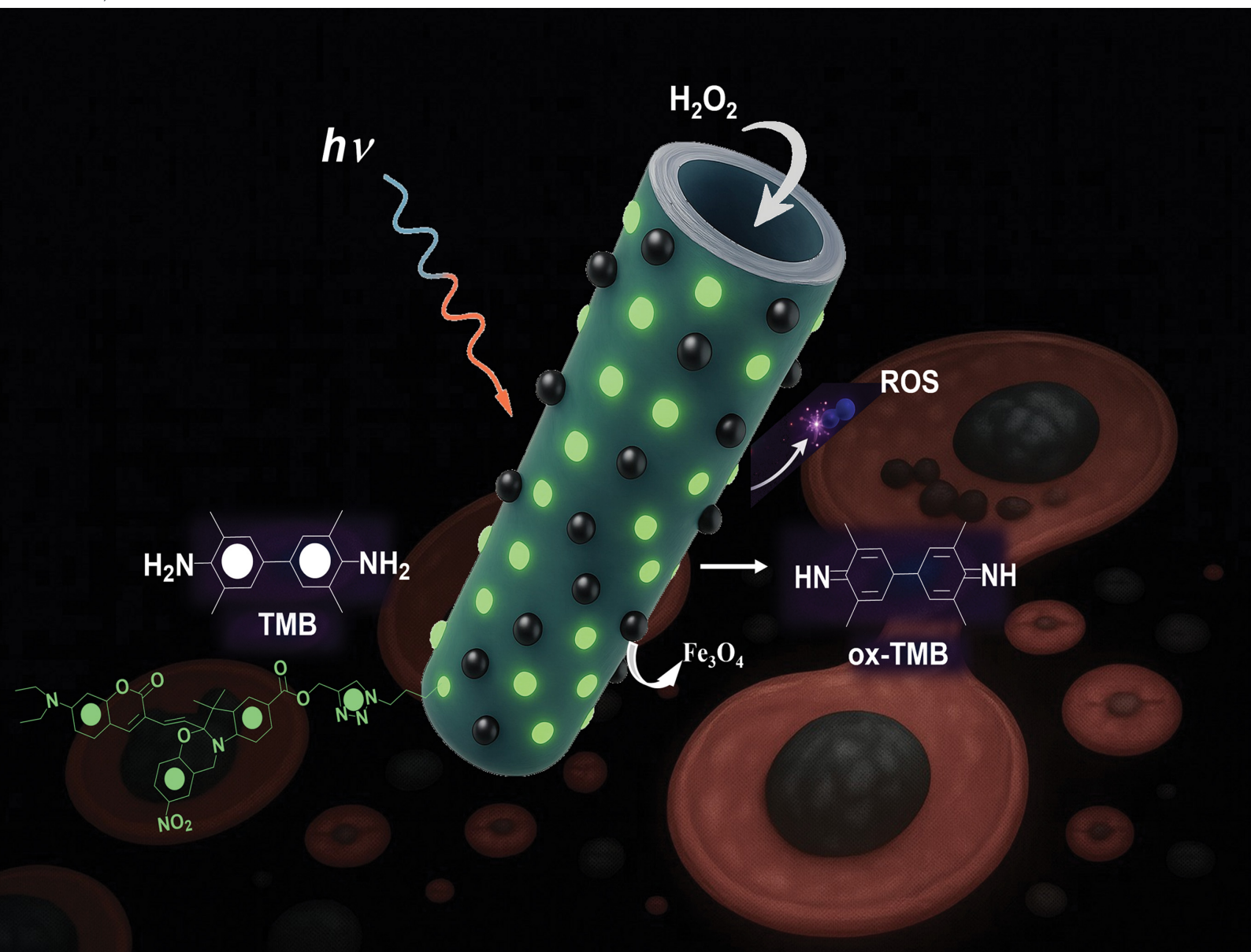
PAPER
Francisco M. Raymo, Serena Riela *et al.*
Design of halloysite nanotube-based nanomaterials
for theranostic applications: fluorescent probes and
chemodynamic activity

PAPER

Check for updates

Design of halloysite nanotube-based nanomaterials for theranostic applications: fluorescent probes and chemodynamic activity†‡

Marina Massaro, [ID] [a] Federica Leone, [ID] [a] Francisco M. Raymo, [ID] *[b]
Raquel de Melo Barbosa, [ID] [c] Rita Sánchez-Espejo, [ID] [d] César Viseras, [ID] [de]
Renato Noto [ID] [a] and Serena Riela [ID] *[f]

The development of theranostic systems is of fundamental importance for the treatment of diseases. These systems should combine the features of fluorescent molecules that can act as diagnostic systems and species with therapeutic potential. Herein, we report the synthesis of a multifunctional halloysite nanotube (HNT)-based nanomaterial *via* the covalent modification of the external surface of the clay with a halochromic probe and the immobilization of Fe_3O_4 nanoparticles (HNTs-**1**@Fe_3O_4) with chemodynamic activity. The covalent modification of HNTs was performed using two different synthetic approaches, and the best strategy was evaluated by estimating the degree of functionalization of the clay *via* thermogravimetric analysis. The synthesized nanomaterial was thoroughly characterized, and its photoluminescence properties under different conditions, *i.e.* different solvents, pH conditions and temperatures, were studied. The HNTs-**1**@Fe_3O_4 nanomaterial was found to exhibit good peroxidase-like activity, as shown by testing its performance in the catalytic oxidation of the colorless enzyme substrate 3,3′,5,5′-tetramethylbenzidine (TMB) to blue TMB oxide (ox-TMB) in the presence of H_2O_2. This study highlights the usefulness of the covalent approach for modifying halloysite surfaces to generate nanomaterials for potential tissue imaging under different stimuli. In addition, the combination with Fe_3O_4NPs led to the synthesis of multifunctional materials with potential use as theranostic systems for the treatment of diseases.

[a] *Dipartimento di Scienze e Tecnologie Biologiche, Chimiche e Farmaceutiche (STEBICEF), Università di Palermo, Viale delle Scienze, Parco d'Orleans II, Ed. 17, 90128 Palermo, Italy*

[b] *Laboratory for Molecular Photonics, Department of Chemistry, University of Miami, Coral Gables, Florida 33146-0431, USA. E-mail: fraymo@miami.edu*

[c] *Department of Pharmacy and Pharmaceutical Technology, School of Pharmacy, University of Seville, C/Professor García González 2, 41012 Sevilla, Spain*

[d] *Department of Pharmacy and Pharmaceutical Technology, Faculty of Pharmacy, University of Granada, Campus Universitario de Cartuja, 18071 Granada, Spain*

[e] *Andalusian Institute of Earth Sciences, CSIC-UGR, 18100 Armilla, Granada, Spain*

[f] *Dipartimento di Scienze Chimiche (DSC), Università di Catania, Viale Andrea Doria 6, 95125 Catania, Italy. E-mail: serena.riela@unict.it*

Introduction

Nowadays, finding systems capable of simultaneously treating and diagnosing various diseases, thus acting as theranostic materials, is challenging.[1,2] Among different techniques that can be used for diagnosis, fluorescence bioimaging is among the most employed for the safe detection of diseases[3] because it is non-invasive and highly sensitive. However, most organic chromophores show low aqueous solubility, which jeopardizes their biological application.[4,5] To overcome this problem, carrier systems that can successfully deliver chromophores to target sites have been proposed.[6] Among the different carrier systems that can be used for these purposes, clay minerals have attracted considerable attention.[7] These minerals, being natural and biocompatible with an innate capacity to be taken up by cells for endocytosis,[8–10] have been used as carrier systems for several hydrophobic species.[11]

Halloysite, an aluminosilicate clay mineral with the general formula $Al_2Si_2O_5(OH)_4 \cdot nH_2O$ is typically found as hollow tubular structures in the nanometer range (often referred to as halloysite nanotubes or HNTs). Because of their empty lumen

This journal is © The Royal Society of Chemistry 2025

J. Mater. Chem. B, 2025, **13**, 9407–9417 | **9407**

and tunable surface chemistry, HNTs hold great potential as carriers for biomedical applications.[12,13] Over the years, different chemical modifications of HNT surfaces[14] have been adopted to obtain promising nanomaterials for the delivery of antioxidants,[15] PNA,[16] chemotherapeutic drugs[17,18] and other active species.[19] In this context, we recently reported the use of halloysites as supramolecular carriers for a halochromic switch for tumor detection (HNTs/**1**).[20] Owing to the presence of HNTs, the probe was successfully internalized by tumoral cell lines, emitting in the red region due to a decrease in the pH. Thus, it possessed potential features for the detection of a tumor environment and therefore for application in the diagnostic field.

In the last years, chemodynamic therapy (CDT), which exploits the production of highly toxic hydroxyl radicals ($^{\bullet}OH$) *via* a Fenton or Fenton-like reaction between a catalyst and H_2O_2 in a tumor microenvironment, has emerged as an innovative approach for cancer treatment.[21,22] Among the different catalysts that can be used for the Fenton reaction, ferroferric oxide nanoparticles (Fe_3O_4NPs) have gained considerable attention in biomedical applications owing to their low toxicity, superparamagnetism, and low cost.[22–24]

Herein, we report the synthesis of a multifunctional halloysite-based nanomaterial as a theranostic system with potential applications in the biomedical field. Firstly, the HNT external surface was covalently modified with a molecular switch (HNTs-**1**) with activatable fluorescence based on the halochromic opening, upon protonation, of oxazine rings.[5,20] The synthesis of this nanomaterial was achieved using two different synthetic approaches, namely, a top-down strategy and a bottom-up one. The first approach was based on the Meldal–Sharpless–Huisgen azide–alkyne 1,3 dipolar cycloaddition between azido-modified HNTs and the previously synthesized halochromic probe bearing a terminal alkyne group, while the second approach involved the step-by-step synthesis of the halochromic probe directly onto the HNT external surface. The more effective synthetic strategy was evaluated by estimating the degree of functionalization of the clay *via* thermogravimetric analysis (TGA). The obtained nanomaterial was thoroughly characterized using different techniques: its colloidal properties were investigated by dynamic light scattering (DLS) measurements, and its morphology was imaged by transmission electron microscopy (TEM) coupled with an EDX probe. Additionally, its photoluminescence properties were studied under different conditions, *i.e.* different solvents, pH and temperatures.

Next, this nanomaterial was used as a scaffold for the immobilization of Fe_3O_4NPs by the co-precipitation method. The amount of Fe_3O_4NPs immobilized onto HNTs-**1** was estimated spectrophotometrically by the thiocyanate method, and the iron oxidation state was verified by X-ray photoelectron spectroscopy (XPS) measurements. The peroxidase-like activity of the prepared nanomaterial was tested in the oxidation of 3,3′,5,5′-tetramethylbenzidine (TMB) as a chemical probe at varying nanomaterial and H_2O_2 concentrations. This study highlights the effectiveness of the covalent approach for modifying halloysite surfaces to obtain HNT-based probes for potential tissue

imaging under different stimuli. In addition, the combination with Fe_3O_4NPs led to the synthesis of multifunctional materials with potential use as theranostic systems for disease treatment.

Experimental section

All reagents used were purchased from Merck (Darmstadt, Germany) and used without further purification. HNTs-N_3 was synthesized as reported elsewhere.[25] **1** was synthesized as reported elsewhere, see the ESI‡ for more details.

The ^1H and ^{13}C NMR spectra were obtained at room temperature using a Bruker Avance II 400 MHz spectrometer.

The thermogravimetric analyses of different nanomaterials were performed on TGA Discovery (TA Instruments). The samples were equilibrated at 50 °C for 20 min; then, measurements were carried out by heating the sample at a rate of 10 °C min^{-1} up to 800 °C.

The FTIR spectra (KBr) were recorded using an Agilent Technologies Cary 630 FT-IR spectrometer. The specimens for these measurements were prepared by mixing 5 mg of the sample powder with 100 mg of KBr.

UV-vis measurements were performed using a Beckmann DU 650 spectrometer. The steady-state and solid-state fluorescence spectra were acquired using a JASCO FP-8300 spectrofluorometer. Excitation and emission slits were 5.0 nm and 2.5 nm, with an emission interval ranging between 400 and 750 nm and excitation wavelengths of 410 nm and 620 nm, respectively.

Transmission electron microscopy (TEM) was performed using a FEI Titan G2 60-300 ultra-high-resolution transmission electron microscope (FEI, Lausanne, Switzerland) coupled with analytical electron microscopy (AEM) performed using a SUPER X silicon drift windowless energy-dispersive X-ray spectroscopy (XEDS) detector. The AEM spectra were saved in mode scanning transmission electron microscopy (STEM) with a high-angle annular dark-field (HAADF) detector.

The DLS and ζ-potential analyses were performed using a Malvern Zetasizer Nano instrument at 25 °C, equipped with a 633-nm solid-state He–Ne laser at a scattering angle of 173°.

X-ray photoelectron spectroscopy (XPS) analyses were carried out using a VG Microtech ESCA 3000 Multilab equipped with a dual Mg/Al anode. For the excitation source, the Al Kα radiation (1486.6 eV) was used. The sample powders were mounted on a double-sided adhesive tape. The pressure in the analysis chamber was in the range of 10^{-8} Torr during data collection.

Synthesis of HNTs-1 *via* the top-down approach

HNTs-N_3 (200 mg) and compound **1** (155 mg) were suspended in a $H_2O/^tBuOH$ (1 : 1) mixture (16 mL). The mixture was stirred in the presence of a catalytic amount of a $CuSO_4\cdot5H_2O$/sodium ascorbate solution (1 M, 1 : 10 v/v) at room temperature for 24 h. After this time, the solvent was filtered, and the powder was rinsed several times with CH_2Cl_2, affording a green powder.

9408 | *J. Mater. Chem. B*, 2025, **13**, 9407–9417

This journal is © The Royal Society of Chemistry 2025

Synthesis of HNTs-2

HNTs-N_3 (200 mg) was suspended in a H_2O/t-BuOH (1:1) mixture (4 mL); then, propargyl alcohol (0.1 mL, 10 eq.) was added. The mixture was stirred under argon in the presence of a catalytic amount of a $CuSO_4 \cdot 5H_2O$/sodium ascorbate solution (1 M, 1:10 v/v) at room temperature for 24 h. After this time, the solvent was filtered, and the powder was rinsed with H_2O and then with MeOH and finally dried at 80 °C under a vacuum, affording a yellow powder.

Synthesis of HNTs-3

A dispersion of HNTs-**2** (500 mg, 0.3 mmol), 2,3,3-trimethyl-5-carboxy-3H-indole (100 mg, 0.5 mmol), DCC (100 mg, 0.5 mmol) and DMAP (60 mg, 0.5 mmol) in CH_2Cl_2 (20 mL) was stirred at room temperature for 48 h. The resulting precipitate was filtered and washed with H_2O, CH_3OH and CH_2Cl_2, affording an orange powder.

Synthesis of HNTs-4

A dispersion of HNTs-**3** (500 mg) and 2-chloromethyl-4-nitrophenol (150 mg, 0.8 mmol) in MeCN (20 mL) was heated under reflux for 72 h. The crude was filtered, washed with MeCN and dried under a vacuum at 60 °C.

Synthesis of HNTs-1 *via* the bottom-up approach

In a round-bottom flask, HNTs-**4** (440 mg), 7-diethylamino-coumarin-3-aldehyde (100 mg, 0.4 mmol) and absolute ethanol (20 mL) were added in the presence of TFA (250 μL). The obtained dispersion was stirred and heated under reflux for 48 h. After this time, the obtained powder was filtered, washed several times with CH_2Cl_2, and dried at 60 °C overnight, affording a green powder.

Synthesis of the HNTs-1@Fe₃O₄ nanomaterial

$FeCl_3$ (135 mg, 0.83 mmol), $FeCl_2 \cdot 4H_2O$ (80 mg, 0.40 mmol), and water (5 mL) were added to a round-bottom flask. For 20 minutes at room temperature, the solution was agitated under inert conditions. After that, the temperature was increased to 80 °C, and 500 mg of HNTs-**1** was added. NH_3 (2 mL) was added after 30 minutes, and the reaction was stirred overnight at 80 °C. A brown powder was formed by filtering the obtained powder and washing it with water, methanol, and CH_2Cl_2.

Loading determination of Fe₃O₄NPs in HNTs-1@Fe₃O₄ by the thiocyanate method

In a round-bottom flask, HNTs-**1**@Fe₃O₄ (50 mg) and aqua regia (5 mL) were heated under reflux for 2 hours. The resulting yellow supernatant was collected and diluted to a final volume of 10 mL. A 0.5-mL aliquot of the supernatant solution was added to a 2-mL aqueous solution of KSCN (0.1 M), and the absorbance of the $[Fe(SCN)]^{2+}$ complex was recorded at λ_{max} = 469 nm. The Fe^{3+} concentration was determined using a calibration curve.

The calibration curve was prepared as follows: different concentrations of $FeCl_3$ (0.4–2 mM) were added in 0.5-mL aliquots to 2 mL of a 0.1 M aqueous KSCN solution. The curve was constructed by plotting the absorbance at λ_{max} = 469 nm against the Fe^{3+} concentration.

Chemodynamic activity

Catalytic oxidation of TMB. The generated •OH from the catalytic decomposition of H_2O_2 by HNTs-**1**@Fe₃O₄ was detected by the colorimetric method using the 3,3′,5,5′-tetramethylbenzidine (TMB) reagent. Different dispersions of the HNTs-**1**@Fe₃O₄ nanomaterial (0.5, 1.0, 2.0 and 4.0 mg mL^{-1}) in a HAc–NaAc buffer (50 mM, pH = 5.5) were prepared in the presence of TMB (1.5 mM) and H_2O_2 (25 mM). The obtained dispersions were incubated under stirring at room temperature under dark conditions for 60 min. At a predetermined time, the dispersions were centrifuged, and the supernatant solutions were analyzed by UV-vis spectroscopy to record the absorbance value at 655 nm.

Afterward, the effect of the H_2O_2 concentration on the production of •OH was investigated. Different concentrations (2.5, 5.0, 7.5, 12.5 and 25.0 mM) of H_2O_2 were added to the dispersions containing TMB (1.5 mM) and HNTs-**1**@Fe₃O₄ (2 mg mL^{-1}); the absorbance at 655 nm was recorded within 60 min using the same procedure as described above.

Catalytic degradation of MB. MB (50 μM) and HNTs-**1**@Fe₃O₄ (0.1 mg mL^{-1}) were mixed in water without or with added H_2O_2 (10 mM). The dispersions were incubated for different times under dark conditions, the powder was deposited at the bottom with a magnet, and the absorbance change for MB at 652 nm was monitored using a UV-vis spectrophotometer.
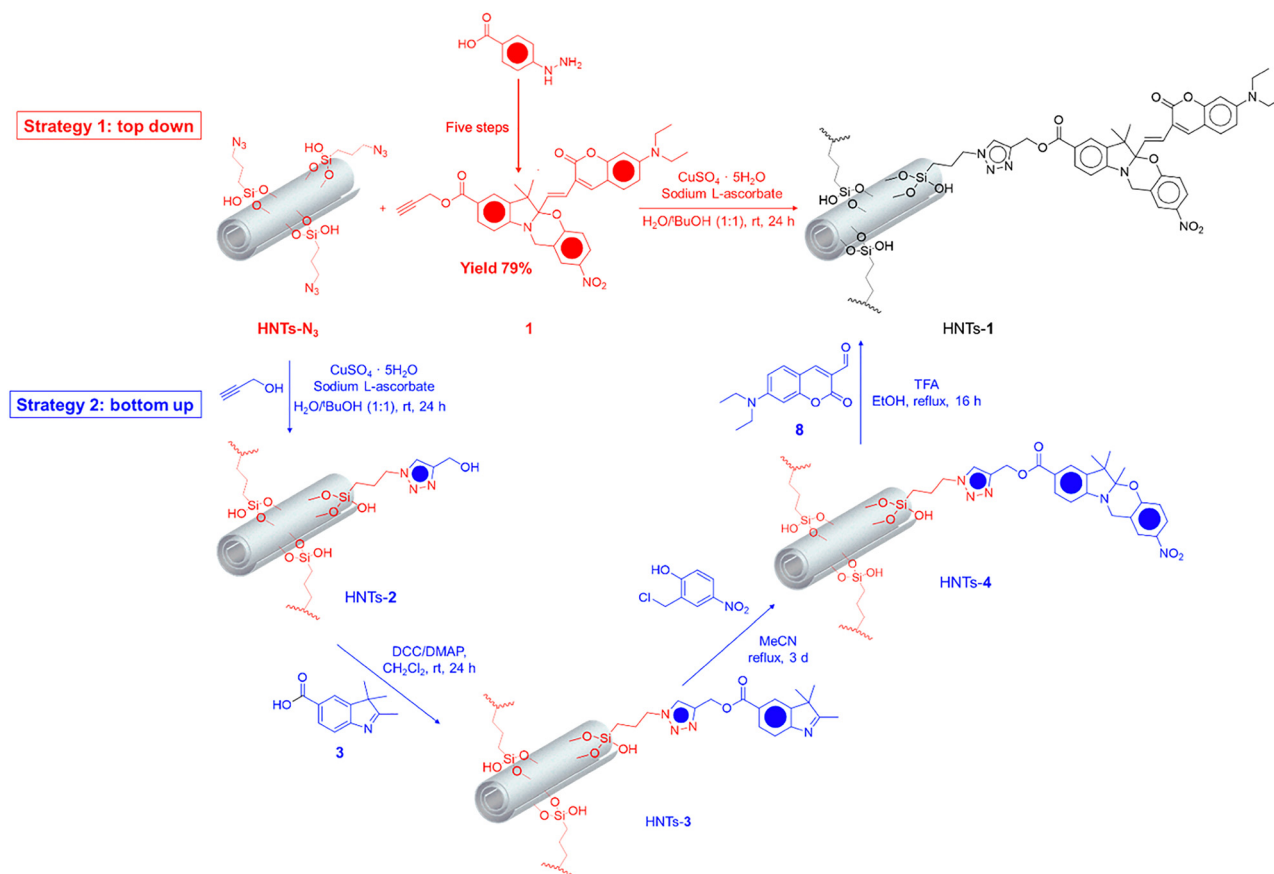
Results and discussion

The synthesis of the potential theranostic system HNTs-**1**@Fe₃O₄ was accomplished in two steps: first, the HNT external surface was covalently modified by linking the fluorescent probe **1**; subsequently, the obtained nanomaterial was loaded with Fe₃O₄ nanoparticles.

Synthesis of the HNTs-1 nanomaterial

For the synthesis of the halloysite-based fluorescent probe (HNTs-**1**), two different approaches were considered, as follows (Scheme 1): (i) a top-down strategy based on the Meldal–Sharpless–Huisgen azide–alkyne 1,3 dipolar cycloaddition between the azido-modified halloysite (HNTs-N_3) and fluorescent compound **1** bearing a terminal alkyne group, previously synthesized[5] (see the ESI‡), was carried out (Scheme 1, strategy 1). The covalent grafting of **1** on HNTs-N_3 was performed at room temperature for 24 h in the presence of $CuSO_4$ and sodium ascorbate as catalysts in a mixture of H_2O/^{t}BuOH (1:1) as the solvent. Then, the obtained HNTs-**1** nanomaterial was isolated as a green powder by subsequent washing of the crude nanomaterial with H_2O and DCM to remove the catalysts and some residual unreacted reagents. On the basis of the stoichiometric ratios between HNTs-N_3 and HNTs-**1** (0.27 mmol g^{-1} and 0.16 mmol g^{-1}, respectively), it was

This journal is © The Royal Society of Chemistry 2025

J. Mater. Chem. B, 2025, **13**, 9407–9417 | **9409**

Scheme 1 Schematic representation of the synthesis of the HNTs-**1** nanomaterial.

determined that the molar ratio between compound **1** and the azido groups of HNTs-N$_3$ bound to the surface of HNTs was 1 : 2. It is worth noting that the complete linkage of compound **1** on the HNT surface is not achieved. This is probably due to steric hindrance, as confirmed by FT-IR spectroscopic investigations (see *infra*). The alternative synthetic approach is (ii) a bottom-up strategy (Scheme 1, strategy 2), in which compound **1** grafted onto the HNT external surface was grown from HNTs-N$_3$ step-by-step using appropriate organic reagents. This approach could be beneficial in terms of the yield and ease of purification.

On account of that, the HNTs-N$_3$ nanomaterial was reacted under "click-chemistry" conditions with propargyl alcohol, affording the HNTs-**2** nanomaterial, in which the full modification of azido groups onto the halloysite was achieved (Table 1). Afterwards, a condensation reaction occurred between HNTs-**2** and 2,3,3-trimethyl-5-carboxy-3H-indole **3**, affording HNTs-**3**. Next, the HNTs-**3** nanomaterial was used as the scaffold for the linkage of 2-chloromethyl-4-nitrophenol by the condensation reaction to obtain the HNTs-**4** nanomaterial, which showed a loading percentage of the organic moiety of *ca.* 3 wt%, as estimated by TGA, corresponding to a degree of functionalization of the HNT surface of 0.20 mmol g^{-1}. Finally, the obtained HNTs-**4** was reacted with the coumarin **8** to achieve the expected HNTs-**1** nanomaterial. It is noteworthy that this latter step was decisive for obtaining the final fluorescent nanomaterial, but unfortunately, the condensation

Table 1 Loading (wt%) and degree of functionalization onto the HNT surface for the synthesis of the HNTs-**1** nanomaterial using the two different approaches

	Nanomaterial	Loading^a (wt%)	Degree of functionalization (mmol g^{-1})
Top-down	HNTs-N$_3$	2.3	0.27 ± 0.02
	HNTs-**1**	7.2	0.16 ± 0.01
Bottom-up	HNTs-**2**	1.5	0.26 ± 0.01
	HNTs-**3**	4.7	0.25 ± 0.01
	HNTs-**4**	3	0.20 ± 0.01
	HNTs-**1**	<1	<0.04

^{a} Calculated using TGA.

reaction between HNTs-**4** and **8** did not afford a satisfactory yield (Table 1). It is possible that because of the steric hindrance on the halloysite surface, the condensation reaction between [1,3]-oxazine, linked onto HNTs in the HNTs-**4** nanomaterial, and coumarin **8** is hampered, justifying the low loading.

Therefore, from these data, it is possible to conclude that the best experimental approach for the synthesis of fluorescent nanomaterials based on the halloysite and **1** is the convergent synthesis, in which the pre-synthesized compound **1** is linked to the HNT external surface. The HNTs-**1** nanomaterial was characterized by FT-IR spectroscopy and TGA, and its colloidal properties were estimated by DLS and ζ-potential measurements.
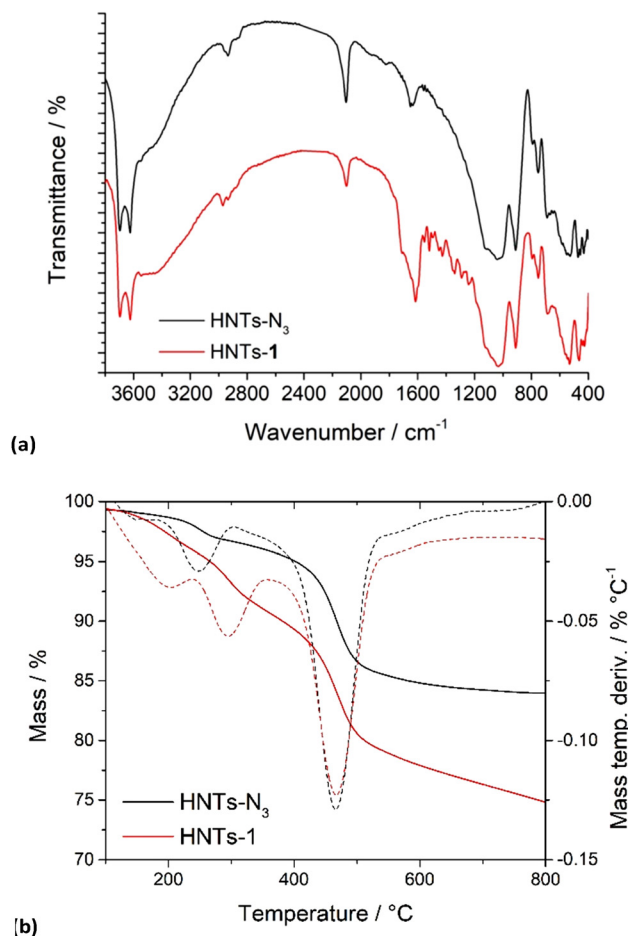
9410 | *J. Mater. Chem. B*, 2025, **13**, 9407–9417

This journal is © The Royal Society of Chemistry 2025

Fig. 1 (a) FT-IR spectra and (b) thermoanalytical curves (solid lines) and their derivatives (dashed lines) of HNTs-N$_3$ and HNTs-**1** nanomaterials.

Furthermore, the morphology of the nanomaterial was imaged by TEM and high-angle annular dark-field scanning transmission electron microscopy (HAADF-STEM). Fig. 1a shows the FT-IR spectra of HNTs-**1** and HNTs-N$_3$ nanomaterials. The assignments for the bands of HNTs-N$_3$ can be done on the basis of the reported data.[25] The FT-IR spectrum of HNTs-**1** exhibits all the bands attributable to the inorganic nanomaterial, and the bands from the organic portion at 2966, 2927, and 2848 cm^{-1} correspond to the asymmetric and symmetric stretching of the methyl and methylene groups, a characteristic band at 1714 cm^{-1} is ascribed to the C=O group, and bands between 1620 and 900 cm^{-1} originate from the stretching and bending of an aromatic ring and C–O and C–N stretching vibrations, respectively. Furthermore, the reduction in the intensity of the typical vibration band of the azido group at *ca.* 2100 cm^{-1} indicates that the click reaction occurs but, according to the degree of functionalization discussed above, some –N$_3$ groups remain unreacted.

Fig. 1b shows the TGA curves of the HNTs-**1** nanomaterial and HNTs-N$_3$ for comparison. As can be seen, besides the typical mass losses of the halloysite arising from the expulsion of the interlayer water molecules of HNTs (*ca.* 550 °C) and those due to the degradation and volatilization of organic matter in HNTs-N$_3$ (*ca.* 250 °C), a two-step degradation pathway was observed in the TGA curve of HNTs-**1**. These mass losses were evidenced by the presence of two peaks, centered at *ca.* 200 and 300 °C, respectively, in the differential thermogravimetric curve, further confirming the successful linkage of **1** onto HNTs.

DLS measurements allow the determination of the structural characteristics of nanomaterials by monitoring their mobility in water and by measuring the average translational diffusion coefficient. This coefficient considers the dimension, shape, and hydration of the diffusing particles, and the existence of aggregation phenomena. By applying the Stokes–Einstein equation, it is possible to calculate the average diameter of the equivalent sphere, which can be used as an index to determine changes in particle dimensions and interparticle aggregation.[26] The HNTs-**1** nanomaterial showed a Z-average size of 485 ± 30 nm, larger than that of pristine HNTs (295 nm),[27] indicating, as expected, that the introduction of a hydrophobic moiety onto the external surface of HNTs led to the synthesis of nanomaterials that showed the worst diffusion in aqueous media. On the contrary, DLS measurements in MeCN revealed a Z-average size of HNTs-**1** (260 ± 7 nm) similar to that of HNTs (240 ± 80 nm) in the same solvent, further confirming the existence of aggregation phenomena in water. The modification of the halloysite external surface was also verified by ζ-potential measurements, which showed that HNTs-**1** possessed a ζ-potential value of −9.20 mV, slightly more negative than that of the HNTs-N$_3$ nanomaterial (−5.35 mV), further confirming the successful linkage of **1**. The morphologies of the different nanomaterials were imaged by TEM and high-angle annular dark-field scanning transmission electron microscopy (HAADF-STEM). The TEM image of the HNTs-**1** nanomaterial (Fig. 2A) showed that the structure of the HNT nanomaterial was preserved after grafting compound **1**. In addition, HNTs-**1** exhibits the characteristic hollow tubular structure of the halloysite, in which the organic molecules are uniformly distributed onto the HNT external surface, as shown by the elemental mapping image highlighting C atoms, extrapolated by energy-dispersive X-ray spectroscopy (EDS). EDS measurements of a selected area also show the presence of C and N atoms, in addition to the typical elements of the halloysite, corroborating the successful synthesis.

Photophysical properties

The UV-vis spectrum of the HNTs-**1** dispersion (0.25 mg mL^{-1} in MeCN) shows an intense absorption maximum at *ca.* 410 nm associated with the coumarin moiety of **1** (Fig. 3a); this spectrum is similar to that of pure compound **1** in MeCN (Fig. S1, ESI‡), indicating that the molecule did not undergo any change in the absorption features after covalent linkage with the HNT nanomaterial.

By changing the pH of the medium and then recording the UV-vis spectrum of the HNTs-**1** dispersion in a MeCN/HCl (3 N) (1 : 1) mixture, we observed a bathochromic shift in the absorption band at *ca.* 200 nm, from 410 to *ca.* 614 nm, due to the protonation of the oxazine ring in HNTs-**1** to form the open-protonated form HNTs-**1OpH** in a similar way to compound **1**

This journal is © The Royal Society of Chemistry 2025

J. Mater. Chem. B, 2025, **13**, 9407–9417 | **9411**
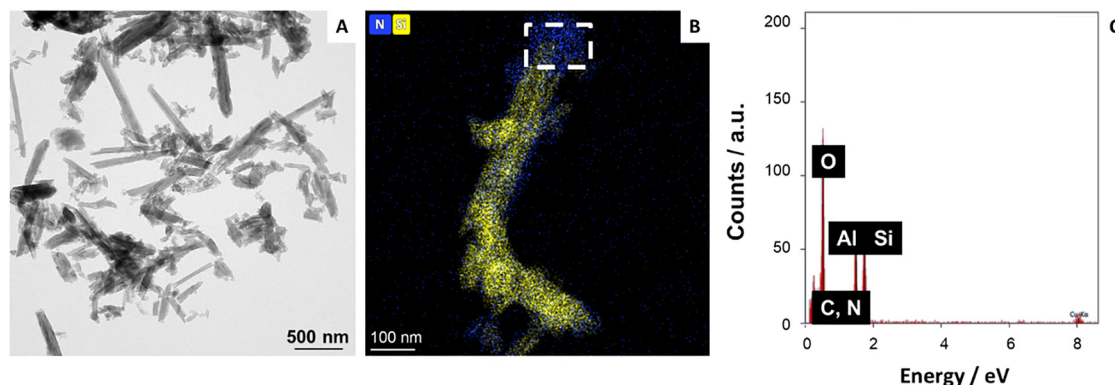
Fig. 2 (A) TEM image of HNTs-**1**, (B) HAADF/STEM of the HNTs-**1** nanomaterial with the elemental mapping images; (C) EDS analysis of the selected area.

(Fig. S1, ESI‡). In addition, the two forms coexist in equilibrium if the UV-vis spectrum of HNTs-**1** is recorded in a MeCN/H$_2$O (1:1) mixture.

By illuminating these dispersions at 410 nm, we observed emissions at *ca.* 470 and 480 nm in MeCN and MeCN/H$_2$O (1:1), respectively, related to the fluorescence of the closed form (Fig. 3A). No emission in this wavelength range was observed by illuminating the HNTs-**1** dispersion in the MeCN/

Fig. 3 (a) Absorption (dashed lines) and emission (solid lines) spectra in different solvents of the HNTs-**1** nanomaterial (0.25 mg mL^{-1}, 298.15 K): MeCN (a and b), H$_2$O/MeCN (1:1) (c and d), and HCl/MeCN (1:1) (e and f). (b) Solid-state fluorescence spectra of **1** and HNTs-**1**.

HCl (1:1) mixture because **1** is completely converted into its protonated form.

Conversely, the illumination of the latter dispersion at 614 nm led to an emission at *ca.* 680 nm, which is associated with the fluorescence of the protonated open form of **1**. Noteworthy, during a comparison of the maximum emission values of the HNTs-**1** nanomaterial with those of pure compound **1** in each solvent used, a hypsochromic shift of *ca.* 10 nm was observed, indicating that the environment surrounding the molecule had changed. However, the solid-state fluorescence spectrum of the HNTs-**1** nanomaterial illuminated at 410 nm is superimposable to that of pure **1** (Fig. 3B).

These results indicate that the HNTs-**1** nanomaterial retains the halochromic properties of pure compound **1**. Thus, it is possible to conclude that, for future clinical applications, the covalent approach is more promising than the supramolecular one because it allows the synthesis of nanomaterials that exhibit fluorescence properties under an external stimulus. In the supramolecular approach, indeed, the intrinsic acidic nature of HNTs causes the oxazine ring in **1** to open, affording the protonated form **1OpH**, and the two species coexist in the HNTs/**1** nanomaterial.

Thus, to fully exploit the nanomaterial peculiarities, the effects of the pH and temperature variations on the absorption/emission features of HNTs-**1** were also investigated.

Firstly, we investigated the effect of the pH on the HNTs-**1** closed and open forms in equilibria. Because the presence of the organic moiety on HNTs-**1** decreases the stability of the dispersion in water compared to pristine HNTs, to better estimate any variation in the absorption and emission features, the spectroscopic properties were investigated in the presence of Pluronic 123, which increases aqueous stability, preserving the photophysical properties.[28] The absorption spectra of the HNTs-**1** nanomaterial acquired at different pH values (Fig. 4a) show the same behavior as pure **1**.

Accordingly, the absorption band intensity of the ring-closed form at 410 nm decreases while that at 620 nm, associated with the protonated ring-open form, increases with decreasing pH. These findings translate into emissions in different ranges of the electromagnetic spectrum (Fig. S2, ESI‡). In particular, by increasing the pH of the dispersion, a decrease in the emission
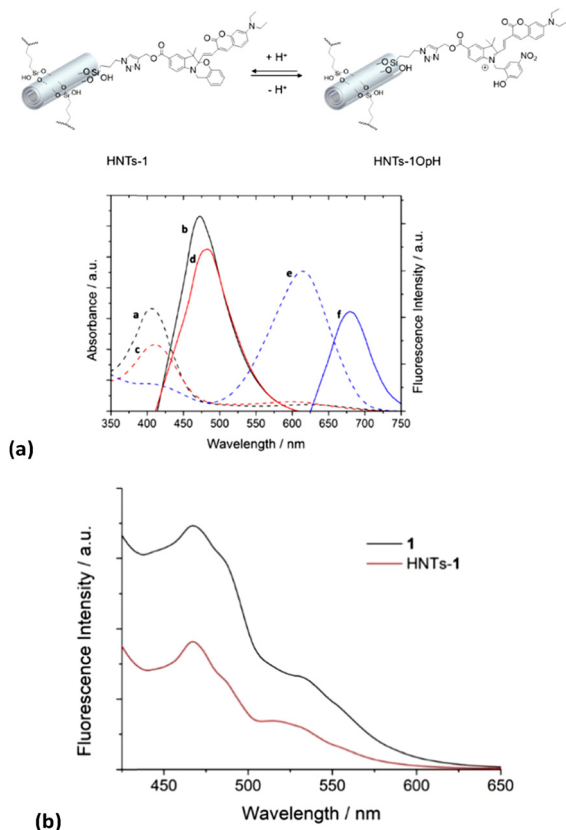
9412 | *J. Mater. Chem. B*, 2025, **13**, 9407–9417

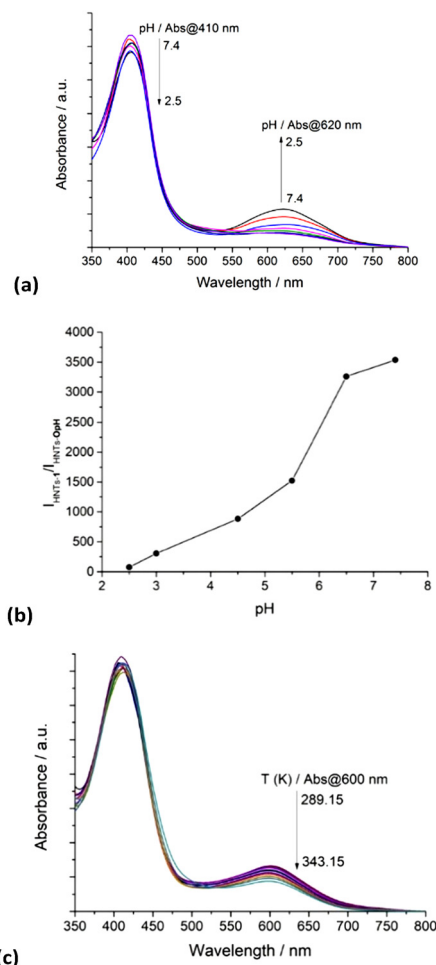This journal is © The Royal Society of Chemistry 2025

Fig. 4 (a) Absorption spectra of the HNTs-**1** dispersion (0.25 mg mL^{-1}) at different pH conditions in the presence of Pluronic 123 at 298.15 K, (b) trend of the ratio between the emission intensities of the ring-closed and ring-open forms of the HNTs-**1** nanomaterial (0.25 mg mL^{-1}) as a function of pH, and (c) absorption spectra of the HNTs-**1** dispersion (0.25 mg mL^{-1}) at different temperatures in a MeCN/H$_2$O (1:1) mixture.

at 650 nm is observed. Similar to that reported in the literature,[28] by plotting the ratio between the emission intensities of the ring-closed form and those of the protonated ring-open species as a function of pH, a monotonic increase is observed (Fig. 4b).

The temperature dependence of the equilibria between the ring-closed and -open forms of the HNTs-**1** nanomaterial was also investigated in the MeCN/H$_2$O (1:1) mixture. Similar to that reported for pure **1**,[29] the absorption spectrum of an equilibrated dispersion of HNTs-**1** at 289.15 K showed the two absorption maxima related to the closed and open isomers; by increasing the temperature from 289.15 to 343.15 K, a decrease of the absorbance of the protonated ring-open form at *ca.* 610 nm was observed and a concomitant slight increase in the absorbance maximum at 410 nm was observed (Fig. 4c).

Synthesis of the HNTs-**1**@Fe$_3$O$_4$ nanomaterial

The synthesis of the HNTs-**1**@Fe$_3$O$_4$ nanomaterial was accomplished by the co-precipitation method (Scheme 2).[30] After work-up, the nanomaterial with approximately 5 wt% Fe$_3$O$_4$NP loading, as estimated by the thiocyanate method, was obtained (see the ESI‡).[31]

The morphology of the HNTs-**1**@Fe$_3$O$_4$ nanomaterial was imaged by transmission electron microscopy (TEM) (Fig. 5A), which showed the uniform distribution of Fe$_3$O$_4$ nanoparticles on the HNTs-**1** surface, as highlighted by the elemental mapping extrapolated by energy-dispersive X-ray spectroscopy (Fig. 5B). The fast Fourier transform of high-magnification HR-TEM indicated nanocrystalline Fe$_3$O$_4$ nanoparticles with a *d* spacing of 0.48 nm, corresponding to the (111) plane of Fe$_3$O$_4$[32] (Fig. 5C). The EDX spectrum from a selected area confirmed the presence of the Fe atoms along with Al, Si, O and C atoms associated with the HNTs-**1** nanomaterial (Fig. 5D). According to statistical analysis, the HNTs-**1**@Fe$_3$O$_4$ nanomaterial showed the presence of Fe$_3$O$_4$ nanoparticles with an average diameter of *ca.* 12.3 ± 2.5 nm (inset in Fig. 5C).

To investigate the valence state of iron in the HNTs-**1**@Fe$_3$O$_4$ nanomaterial, XPS measurements were performed. Fig. 5E shows the characteristic peaks located at *ca.* 711.7 and 725.2 eV, corresponding to the binding energies of Fe 2p$_{3/2}$ and Fe 2p$_{1/2}$, respectively, along with satellite peaks at 719.1 eV and 733.0 eV. The Fe 2p$_{2/3}$ peak for Fe$_3$O$_4$ was deconvoluted into two components at 711.4 eV and 713.7 eV. The relative areas of the deconvoluted peaks assigned to Fe^{2+} and Fe^{3+} were calculated to be 0.28:0.71, closely matching the stoichiometric Fe^{2+}/Fe^{3+} ratio of Fe$_3$O$_4$.[33] The Fe 2p$_{1/2}$ peak was also deconvoluted into two peaks at 724.9 eV and 727.0 eV.[34,35]
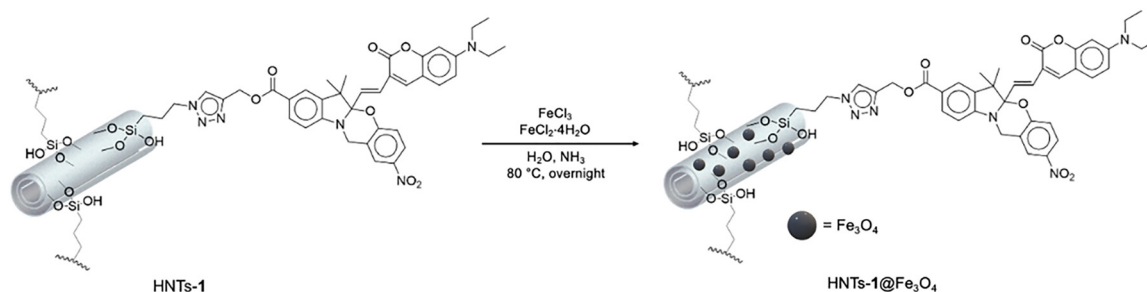
Scheme 2 Schematic representation of the synthesis of the HNTs-**1**@Fe$_3$O$_4$ nanomaterial.

This journal is © The Royal Society of Chemistry 2025

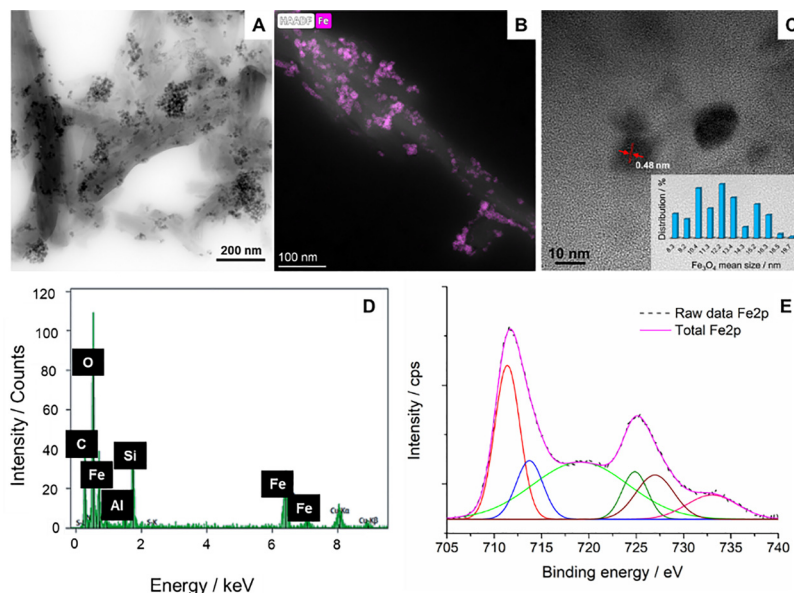*J. Mater. Chem. B*, 2025, **13**, 9407–9417 | **9413**

Fig. 5   (A) TEM, (B) HAADF/STEM image with Fe elemental mapping and (C) HR-TEM image of the HNTs-**1**@Fe$_3$O$_4$ nanomaterial. The inset shows the diameter size distribution (number of counts = 215). (D) EDX analysis. (E) Deconvoluted Fe 2p spectrum from XPS analysis.

The peroxidase-like activity of the synthesized nanomaterial was evaluated using the catalytic oxidation of 3,3′,5,5′-tetramethylbenzidine (TMB), a peroxidase substrate. This molecule can indeed be oxidized by ROS to afford ox-TMB, which shows a specific absorbance at 655 nm.[36] As shown in Fig. 6, in the presence of H$_2$O$_2$ (25 mM) at pH = 5.5, the oxidation of TMB by the HNTs-**1**@Fe$_3$O$_4$ nanomaterial (Fig. 6a) is time- and concentration-dependent. In particular, Fig. 6b shows the variation in the UV-vis absorbance intensity of ox-TMB in the presence of the HNTs-**1**@Fe$_3$O$_4$ nanomaterial (2.0 mg mL^{-1}) and H$_2$O$_2$ (25 mM) as a function of time, indicating that the nanomaterials induced effects on ROS generation, presumably $^\bullet$OH or $^\bullet$O$_2^-$,[37,38] which increased with increasing concentration (from 0.5 to 4.0 mg mL^{-1}), as shown in Fig. 6c.

Furthermore, the production of ROS is H$_2$O$_2$-dependent (Fig. S5, ESI‡), and exposure to high concentrations of H$_2$O$_2$ (ranging from 0 to 25 mM) generates increased levels of ROS with faster reaction kinetics, as determined by the Michaelis–Menten kinetics (Fig. 6d) and Lineweaver–Burk plot fitting (Fig. S6, ESI‡). The Michaelis constant (K_m) and the maximal reaction rate (V_{max}) of the HNTs-**1**@Fe$_3$O$_4$ nanomaterial at room temperature were determined to be 8.5 ± 0.9 mM and $(7.9 ± 0.4) × 10^{-9}$ M s^{-1}, respectively, which are comparable to those of the well-studied Fe$_3$O$_4$ nanozyme and the natural horseradish peroxidase (Table 2).

Finally, to find the optimal experimental conditions, the absorbance of the system was investigated at different pH (3.5–7.0). As shown in Fig. 6e, the pH influences the peroxidase-like activity of HNTs-**1**@Fe$_3$O$_4$. It was indeed found that the activity of the nanomaterial first increases and then decreases with increasing pH of the medium, allowing us to conclude that the optimal pH is 4.5.

ROS generation was also confirmed by adding the HNTs-**1**@Fe$_3$O$_4$ nanomaterial to an H$_2$O$_2$ solution (pH = 5.5)

containing methylene blue (MB).[33] In Fig. 6f, the trend of MB absorbance as a function of time in the presence of H$_2$O$_2$ and the HNTs-**1**@Fe$_3$O$_4$ nanomaterial (0.1 mg mL^{-1}) is shown. As can be seen, a decrease in the typical absorption band of MB is observed, indicating that the degradation of MB occurs *via* ROS. The inset in Fig. 6e shows the trend of the absorbance at 655 nm, normalized to account for the amount of MB absorbed on the nanomaterial. It should be noted that under the same experimental conditions, a small portion of MB is adsorbed onto the HNTs-**1**@Fe$_3$O$_4$ nanomaterial due to favorable electrostatic interactions between the positively charged MB and the negatively charged external surface of HNTs-**1**@Fe$_3$O$_4$; hence, the absorbance of MB decreases even in the absence of H$_2$O$_2$ (Fig. S7, ESI‡).

Conclusions

This study exploited the usefulness of the covalent approach to modify halloysite surfaces, generating a HNT-based probe for potential tissue imaging under different stimuli. Furthermore, its combination with Fe$_3$O$_4$NPs led to the synthesis of multifunctional materials with potential application as theranostic systems for the treatment of diseases.

To achieve this objective, the HNT external surface was covalently modified using two different synthetic approaches: a top-down strategy based on the Meldal–Sharpless–Huisgen azide–alkyne 1,3 dipolar cycloaddition between azido-modified HNTs and a halochromic probe bearing a terminal alkyne group, which was previously synthesized, and a bottom-up approach, in which the halochromic probe was synthesized step-by-step directly onto the HNT external surface. The best synthetic strategy was evaluated by estimating the degree of

9414 | *J. Mater. Chem. B*, 2025, **13**, 9407–9417

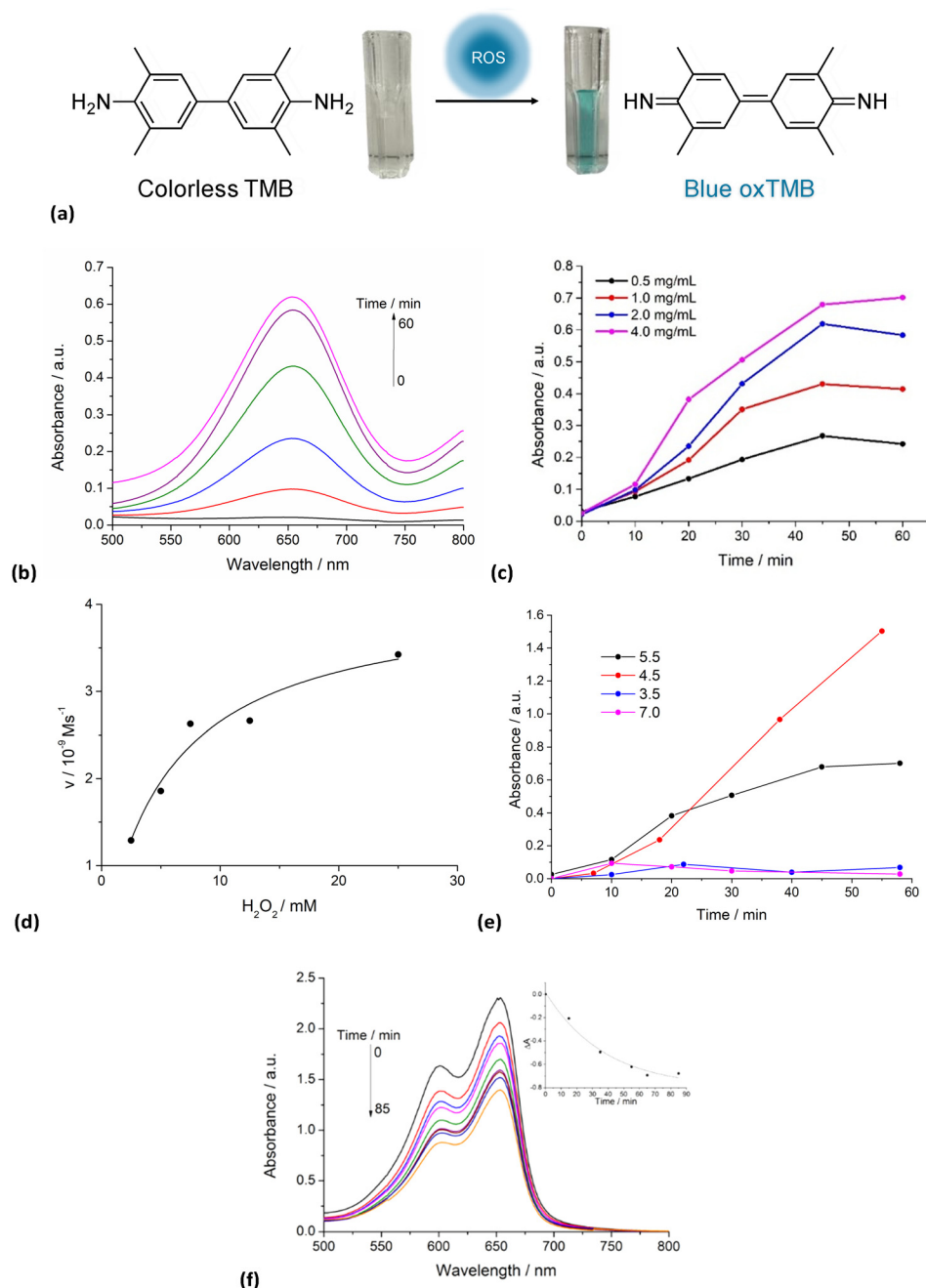This journal is © The Royal Society of Chemistry 2025

Fig. 6 (a) Schematic of the TMB oxidation process by ROS generated from the Fenton reaction, (b) time-dependent oxidation of TMB induced by ROS generation from the HNTs-**1**@Fe$_3$O$_4$ nanomaterial (2.0 mg mL^{-1}) with 25 mM H$_2$O$_2$, (c) time-course chemodynamic activity of the HNTs-**1**@Fe$_3$O$_4$ nanomaterial at different concentrations, (d) Michaelis–Menten kinetics, (e) pH-dependent oxidation of TMB induced by ROS generation from the HNTs-**1**@Fe$_3$O$_4$ nanomaterial (4.0 mg mL^{-1}) with 25 mM H$_2$O$_2$, and (f) trend of the maximum absorption band of MB as a function of the time in the presence of the HNTs-**1**@Fe$_3$O$_4$ nanomaterial (0.1 mg mL^{-1}) and H$_2$O$_2$ (10 mM). The inset shows the trend of the normalized absorbance as a function of time.

functionalization of the clay using TGA, which showed that the best experimental approach for this type of synthesis is the convergent one, where the pre-synthesized compound **1** is linked to the HNT external surface. The successful modification was verified by FT-IR spectroscopy and TGA and DLS measurements. The latter showed the presence of aggregates, which diffuse in aqueous media, due to the introduction of **1**. Morphological investigations showed that HNTs-**1** exhibits

the characteristic hollow tubular structure of halloysites, with organic molecules uniformly distributed on the HNT external surface, as shown by elemental mapping. The photoluminescence studies of HNTs-**1** indicated that it retains all spectroscopic properties of the pure molecule under all conditions investigated. The introduction of Fe$_3$O$_4$ nanoparticles onto the HNTs-**1** nanomaterial confers chemodynamic properties to the clay, as shown by the catalytic oxidation of TMB in the presence

This journal is © The Royal Society of Chemistry 2025

J. Mater. Chem. B, 2025, **13**, 9407–9417 | **9415**

Table 2 Comparison of the kinetic parameters (K_m and V_{max}) of a natural enzyme and different nanozymes

	K_m/mM	$V_{max}/10^{-8}$ M s^{-1}	Ref.
Fe$_3$O$_4$	154	3.44	39
HRP	3.7	8.71	39
Ag@Fe$_3$O$_4$	75.2	2.28	40
Casein-Fe$_3$O$_4$	4.75	15.9	41
Fe-CDs	97.64	0.424	42
HNTs-**1**@Fe$_3$O$_4$	8.5	0.8	This work

of H$_2$O$_2$. By fitting the experimental data obtained by varying the concentration of H$_2$O$_2$ as a function of time with the Michaelis–Menten model, the Michaelis constant (K_m) and maximal reaction rate (V_{max}) of the HNTs-**1**@Fe$_3$O$_4$ nanomaterial at room temperature were determined to be 8.5 ± 0.9 mM and $(7.9 \pm 0.4) \times 10^{-9}$ M s^{-1}, respectively, which are comparable to those of the well-studied Fe$_3$O$_4$ nanozyme and natural horseradish peroxidase.

Thus, the developed nanomaterial possesses interesting theranostic properties for future applications in the treatment of diseases. Considering the non-biodegradability of halloysites, it is possible to hypothesize future applications of the developed systems in oral, topical, or local administration for the treatment, for example, of solid tumors.

Author contributions

Marina Massaro: formal analysis, methodology, investigation, writing – original draft, and writing – review and editing. Federica Leone: investigation, formal analysis, methodology, and writing–original draft. Francisco M. Raymo: conceptualization, investigation, formal analysis, resources, writing–original draft, and writing – review and editing. Raquel de Melo Barbosa: formal analysis and methodology. Rita Sánchez-Espejo: formal analysis and methodology. Cèsar Viseras: formal analysis and resources. Renato Noto: formal analysis. Serena Riela: conceptualization, supervision, methodology, formal analysis, resources, writing – original draft, and writing – review and editing.

Conflicts of interest

There are no conflicts to declare.

Data availability

No primary research results, software or code has been included, and no new data were generated or analysed as part of this review.

Acknowledgements

Notes and references

1 O. Taratula, C. Schumann, M. A. Naleway, A. J. Pang, K. J. Chon and O. Taratula, *Mol. Pharm.*, 2013, **10**, 3946–3958.

2 A. Demiral, N. Verimli, S. İ. Goralı, H. Yılmaz, M. Çulha and S. S. Erdem, *J. Photochem. Photobiol., B*, 2021, **222**, 112261.

3 H.-S. Peng and D. T. Chiu, *Chem. Soc. Rev.*, 2015, **44**, 4699–4722.

4 J. Cusido, M. Battal, E. Deniz, I. Yildiz, S. Sortino and F. M. Raymo, *Chem. – Eur. J.*, 2012, **18**, 10399–10407.

5 S. Tang, Y. Zhang, E. R. Thapaliya, A. S. Brown, J. N. Wilson and F. M. Raymo, *ACS Sens.*, 2017, **2**, 92–101.

6 Y. Zhang, S. Swaminathan, S. Tang, J. Garcia-Amorós, M. Boulina, B. Captain, J. D. Baker and F. M. Raymo, *J. Am. Chem. Soc.*, 2015, **137**, 4709–4719.

7 M. Massaro, S. Pieraccini, S. Guernelli, M. L. Dindo, S. Francati, L. F. Liotta, G. C. Colletti, S. Masiero and S. Riela, *Appl. Clay Sci.*, 2022, **230**, 106719.

8 M. Notarbartolo, M. Massaro, R. de Melo Barbosa, C. Emili, L. F. Liotta, P. Poma, F. M. Raymo, R. Sànchez-Espejo, R. Vago, C. Viseras-Iborra and S. Riela, *Colloids Surf., B*, 2022, **220**, 112931.

9 G. Biddeci, G. Spinelli, M. Massaro, S. Riela, P. Bonaccorsi, A. Barattucci and F. Di Blasi, *Int. J. Nanomed.*, 2021, **16**, 4755–4768.

10 E. Rozhina, A. Panchal, F. Akhatova, Y. Lvov and R. Fakhrullin, *Appl. Clay Sci.*, 2020, **185**, 105371.

11 M. Massaro, S. Riela, C. Baiamonte, J. L. J. Blanco, C. Giordano, P. Lo Meo, S. Milioto, R. Noto, F. Parisi, G. Pizzolanti and G. Lazzara, *RSC Adv.*, 2016, **6**, 87935–87944.

12 A. C. Santos, I. Pereira, S. Reis, F. Veiga, M. Saleh and Y. Lvov, *Expert Opin. Drug Delivery*, 2019, **16**, 1169–1182.

13 D. Peixoto, I. Pereira, M. Pereira-Silva, F. Veiga, M. R. Hamblin, Y. Lvov, M. Liu and A. C. Paiva-Santos, *Coord. Chem. Rev.*, 2021, **440**, 213956.

14 A. Stavitskaya, M. Rubtsova, A. Glotov, V. Vinokurov, A. Vutolkina, R. Fakhrullin and Y. Lvov, *Nanoscale Adv.*, 2022, **4**, 2823–2835.

15 Z. Yao, W. Gong, C. Li, Z. Deng, Y. Jin and X. Meng, *J. Appl. Polym. Sci.*, 2023, **140**, e53411.

16 M. Massaro, E. Licandro, S. Cauteruccio, G. Lazzara, L. F. Liotta, M. Notarbartolo, F. M. Raymo, R. Sánchez-Espejo, C. Viseras-Iborra and S. Riela, *J. Colloid Interface Sci.*, 2022, **620**, 221–233.

17 X. Luo, J. Zhang, Y.-P. Wu, X. Yang, X.-P. Kuang, W.-X. Li, Y.-F. Li, R.-R. He and M. Liu, *ACS Biomater. Sci. Eng.*, 2020, **6**, 3361–3374.

9416 | *J. Mater. Chem. B*, 2025, **13**, 9407–9417

This journal is © The Royal Society of Chemistry 2025

18 M. Massaro, P. Poma, G. Cavallaro, F. García-Villén, G. Lazzara, M. Notarbartolo, N. Muratore, R. Sánchez-Espejo, C. Viseras Iborra and S. Riela, *Colloids Surf., B*, 2022, **213**, 112385.

19 Z. Long, Y.-P. Wu, H.-Y. Gao, Y.-F. Li, R.-R. He and M. Liu, *Bioconjugate Chem.*, 2018, **29**, 2606–2618.

20 M. Massaro, M. Notarbartolo, F. M. Raymo, G. Cavallaro, G. Lazzara, M. M. A. Mazza, C. Viseras-Iborra and S. Riela, *ACS Appl. Nano Mater.*, 2022, **5**, 13729–13736.

21 Y. Deng, M. Ding, L. Zhu, Y. Zhang, F. Wang, L. Zhao and J. Li, *J. Mater. Chem. B*, 2023, **11**, 8484–8491.

22 Y. Wang, X. Li, Y. Fang, J. Wang, D. Yan and B. Chang, *RSC Adv.*, 2023, **13**, 7952–7962.

23 Z. Shen, T. Liu, Y. Li, J. Lau, Z. Yang, W. Fan, Z. Zhou, C. Shi, C. Ke, V. I. Bregadze, S. K. Mandal, Y. Liu, Z. Li, T. Xue, G. Zhu, J. Munasinghe, G. Niu, A. Wu and X. Chen, *ACS Nano*, 2018, **12**, 11355–11365.

24 W. Wang, Z. Huang, Y. Huang, X. Pan and C. Wu, *Int. J. Pharm.*, 2020, **589**, 119815.

25 M. Massaro, P. Poma, C. G. Colletti, A. Barattucci, P. M. Bonaccorsi, G. Lazzara, G. Nicotra, F. Parisi, T. M. G. Salerno, C. Spinella and S. Riela, *Appl. Clay Sci.*, 2020, **184**, 105400.

26 M. L. Alfieri, M. Massaro, M. d'Ischia, G. D'Errico, N. Gallucci, M. Gruttadauria, M. Licciardi, L. F. Liotta, G. Nicotra, G. Sfuncia and S. Riela, *J. Colloid Interface Sci.*, 2022, **606**, 1779–1791.

27 M. Massaro, G. Cinà, G. Cavallaro, G. Lazzara, A. Silvestri, R. D. M. Barbosa, R. Sànchez-Espejo, C. Viseras-Iborra, M. Notarbartolo and S. Riela, *Int. J. Mol. Sci.*, 2024, **25**, 5370.

28 M. M. A. Mazza, F. Cardano, J. D. Baker, S. Giordani and F. M. Raymo, *Front. Mater.*, 2021, **8**, 630046.

29 Y. Zheng, Y. Meana, M. M. A. Mazza, J. D. Baker, P. J. Minnett and F. M. Raymo, *J. Am. Chem. Soc.*, 2022, **144**, 4759–4763.

30 Y. Xie, D. Qian, D. Wu and X. Ma, *Chem. Eng. J.*, 2011, **168**, 959–963.

31 C. Verma, K. Tapadia and A. B. Soni, *Food Chem.*, 2017, **221**, 1415–1420.

32 D. Mohanta and M. Ahmaruzzaman, *Chemosphere*, 2021, **285**, 131395.

33 Y. Yang, P. Wang, R. Shi, Z. Zhao, A. Xie, Y. Shen and M. Zhu, *Chem. Eng. J.*, 2022, **441**, 136042.

34 T. Missana, C. Maffiotte and M. García-Gutiérrez, *J. Colloid Interface Sci.*, 2003, **261**, 154–160.

35 N. Wang, M. Wang, H. Quan, S. Wang and D. Chen, *Sep. Purif. Technol.*, 2024, **329**, 125184.

36 W. Du, T. Liu, F. Xue, X. Cai, Q. Chen, Y. Zheng and H. Chen, *ACS Appl. Mater. Interfaces*, 2020, **12**, 19285–19294.

37 X. Zhu, P. Song, S. Hou, H. Zhao, Y. Gao, T. Wu and Q. Liu, *Appl. Clay Sci.*, 2023, **242**, 107022.

38 P. Song, S. Hou, B. Gong, J. Zhao, M. Zhu, H. Liu, H. Zhao, T. Wu, X. Zhu and Q. Liu, *Inorg. Chem. Commun.*, 2024, **165**, 112508.

39 L. Gao, J. Zhuang, L. Nie, J. Zhang, Y. Zhang, N. Gu, T. Wang, J. Feng, D. Yang, S. Perrett and X. Yan, *Nat. Nanotechnol.*, 2007, **2**, 577–583.

40 J. Chen, Y. Liu, G. Zhu and A. Yuan, *Cryst. Res. Technol.*, 2014, **49**, 309–314.

41 Y. Liu, M. Yuan, L. Qiao and R. Guo, *Biosens. Bioelectron.*, 2014, **52**, 391–396.

42 Y. Liu, B. Xu, M. Lu, S. Li, J. Guo, F. Chen, X. Xiong, Z. Yin, H. Liu and D. Zhou, *Bioact. Mater.*, 2022, **12**, 246–256.

This journal is © The Royal Society of Chemistry 2025

J. Mater. Chem. B, 2025, **13**, 9407–9417 | **9417**